Supplement material for our paper titled "Development High-order Global Dynamical Core using Discontinuous Galerkin Method for atmospheric LES and proposal of test cases"

Yuta Kawai[1] and Hirofumi Tomita[1,2]

[1]RIKEN Center for Computational Science, Kobe, Japan.
[2]RIKEN Cluster for Pioneering Research, Wako, Japan

May 17, 2024

1 Additional information for mountain wave test

In this section, we detail the spin-up strategy and sponge layer, which were used in the mountain wave test described in Sect. 3.3 of our paper. In addition, we consider some reasons why the obtained convergence rate is slightly less than the optimal order accuracy.

1.1 Spin-up strategy

To mitigate the influence of impulsive start on numerical solutions, we gradually accelerated the wind as performed in previous studies with regional experimental setup. The initial condition is a rest isothermal atmosphere and is represented as

$$u^\xi = 0,\ u^\zeta = 0,\ u^\eta = 0,$$
$$p = P_0 \exp\left(-\frac{gz}{RT_0}\right),$$
$$\rho = \frac{P_0}{RT_0} \exp\left(-\frac{gz}{RT_0}\right), \tag{S1}$$

where $P_0 = 10^5$ Pa and $T_0 = 300$ K. To accelerate a zonal wind, we added the relaxation terms in the right-hand side of governing equations as

$$\frac{\partial \sqrt{G}\rho'}{\partial t} = \cdots - \alpha_f \sqrt{G}\rho',$$
$$\frac{\partial \sqrt{G}\rho u^\xi}{\partial t} = \cdots - \alpha_f \sqrt{G}\left(\rho u^\xi - \rho U^\xi\right),$$
$$\frac{\partial \sqrt{G}\rho u^\eta}{\partial t} = \cdots - \alpha_f \sqrt{G}\left(\rho u^\eta - \rho U^\eta\right),$$
$$\frac{\partial \sqrt{G}\rho u^\zeta}{\partial t} = \cdots - \alpha_f \sqrt{G}\left(\rho u^\zeta - \rho U^\zeta\right), \tag{S2}$$
$$\frac{\partial \sqrt{G}(\rho\theta)'}{\partial t} = \cdots - \alpha_f \sqrt{G}(\rho\theta)',$$

where (U^ξ, U^η, U^ζ) are the vector components of prescribed wind and α_f is a time-dependent coefficient with Rayleigh forcing terms. Note that we set the hydrostatic balance part of pressure and density as

$$p_{\text{hyd}} = P_0 \exp\left(-\frac{u_{\text{eq}}}{2RT_0}\sin^2\theta - \frac{gz}{RT_0}\right), \quad \rho_{\text{hyd}} = \frac{p_{\text{hyd}}}{RT_0},$$

which satisfies a dynamically balanced state associated with a zonal wind in solid rotation, $u_{\text{eq}}\cos\theta$. Then, the perturbation at the initial time is given by $p' = p - p_{\text{hyd}}$, $\rho' = \rho - \rho_{\text{hyd}}$.

As the horizontal component of prescribed wind, we consider a zonal wind in solid body rotation where $u_{\text{eq}} = 20$ m/s. The corresponding (U^ξ, U^η) can be calculated by considering the coordinate conversion between the cubed-sphere and geographic coordinates. To improve the inconsistency with no-flux boundary condition at the surface, we add the vertical component in the form of

$$U^\zeta = -\sqrt{G}_v(G_v^{13}U^\xi + G_v^{23}U^\eta)\exp\left(-\frac{\zeta}{H_f}\right),$$

where H_f was set to 2 km in this study. This modification also reduces the influence of initial shock. On the other hand, the coefficient with the forcing terms is given as $\alpha_f(t) = w(t)\tau_f^{-1}$, where

$$
\begin{aligned}
w &= 1 && \text{for } 0 \leq t \leq t_1, \\
w &= \frac{1}{2}\left[1 - \cos\left(\pi\frac{t - t_1}{t_2 - t_1}\right)\right] && \text{for } t_1 \leq t \leq t_2, \\
w &= 0 && \text{for } t \geq t_2,
\end{aligned}
$$

and τ_f is the forcing time scale. In this study, these parameters were set as $\tau_f = 60$ s, $t_1 = 200$ s, and $t_2 = 1800$ s.

1.2 Sponge layer

To suppress a reflection of waves at the model top, we introduced a sponge layer at upper computational domain. In addition, to reduce the disruption of our targeting structure of mountain wave due to the global propagation of initial shocks, a lateral sponge layer was placed on the 1/4 sector of the sphere. As in Eq. (S2), linear damping terms were added to the governing equations as follows:

$$
\begin{aligned}
\frac{\partial \sqrt{G}\rho'}{\partial t} &= \cdots - \alpha_s\sqrt{G}\rho', \\
\frac{\partial \sqrt{G}\rho u^\xi}{\partial t} &= \cdots - \alpha_s\sqrt{G}\left(\rho u^\xi - U^\xi\right), \\
\frac{\partial \sqrt{G}\rho u^\eta}{\partial t} &= \cdots - \alpha_s\sqrt{G}\left(\rho u^\eta - \rho U^\eta\right), \\
\frac{\partial \sqrt{G}\rho u^\zeta}{\partial t} &= \cdots - \alpha_s\sqrt{G}\left(\rho u^\zeta - \rho U^\zeta\right), \\
\frac{\partial \sqrt{G}(\rho\theta)'}{\partial t} &= \cdots - \alpha_s\sqrt{G}(\rho\theta)'.
\end{aligned}
$$

The decay coefficient is given as $\alpha_s = (1 - w(t))(\alpha_{s,h} + \alpha_{s,v})$ where $\alpha_{s,h}$ and $\alpha_{s,v}$ are the coefficients for lateral and upper sponge layers, respectively. To avoid the sponge layer interfering with the initial forcing in Eq. (S2), as the initial forcing weakens, the sponge layer is gradually activated using the coefficient $(1 - w(t))$. The coefficient for the upper sponge layer is given as

$$\alpha_{s,v} = \frac{\tau_{s,v}^{-1}}{2}\left\{\frac{1}{2}\left[1 + \tanh\left(\frac{z - (z_T + z_{\text{sp}})/2}{\delta_{\text{sp},v}(z_T - z_{\text{sp}})}\right)\right]\right\},$$
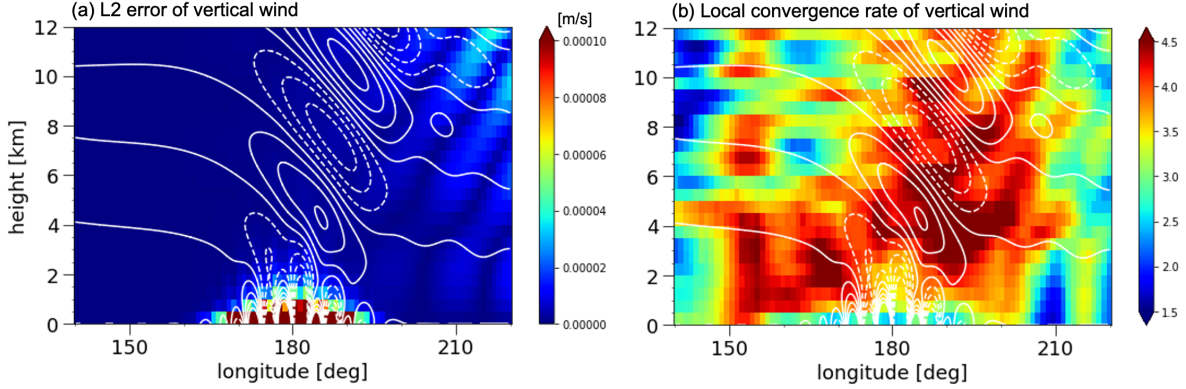
2

Figure S1: After 2 hours in a mountain wave test case with global model, spatial distribution of (a) L_2 error norm and (b) local convergence rate for the vertical wind at the equator in the case where the effective horizontal and vertical grid spacing $\Delta_{\mathrm{eff},h}, \Delta_{\mathrm{eff},v}$ is set to 156 m and 125 m, respectively, using $p = 3$. When evaluating the local convergence rate, we used the results obtained from two experiments: a coarse resolution experiment ($\Delta_{\mathrm{eff},h} = 625$ m, $\Delta_{\mathrm{eff},v} = 500$ m) and the highest resolution experiment for $p = 3$ ($\Delta_{\mathrm{eff},h} = 156$ m, $\Delta_{\mathrm{eff},v} = 125$ m). In each figure, the white lines represent the vertical wind in the highest resolution experiment for $p = 3$.

whereas, for the lateral sponge layer,

$$
\alpha_{s,h} = \frac{\tau_{s,h}^{-1}}{2} \left\{ \left[1 - \tanh\left(\frac{\lambda - \pi/4}{\delta_{\mathrm{sp},h}\pi/2} \right) \right] + \left[1 + \tanh\left(\frac{\lambda - 7\pi/4}{\delta_{\mathrm{sp},h}\pi/2} \right) \right] \right\}
$$
$$
\cdot \frac{1}{2} \left[1 + \tanh\left(\frac{|\theta| - \pi/3}{8\pi/180} \right) \right],
$$

where z_T is the height of model top, and $\tau^{s,v}$ and $\tau^{s,h}$ are the decay time scales corresponding to the upper and lateral sponge layers. Note that the coefficient for the lateral sponge layer is multiplied by a tapering function in the latitudinal direction to avoid an infinite zonal scale near the poles, as performed in Eq. (20) of our paper. In this study, we set $z_{\mathrm{sp}} = 15$ km, $\delta_{\mathrm{sp},v} = \delta_{\mathrm{sp},h} = 0.16$, and $\tau_{s,v} = \tau_{s,h} = 100$ s.

1.3 Investigation of degrading the optimal numerical convergence

Figure 5 of our paper indicates that the convergence rate obtained from the mountain test case is slightly smaller than $p + 1$-order accuracy. We consider the reasons behind this result to be as follows; First, to evaluate the differentials with the Jacobian cofactors ($\sqrt{G_v}G_v^{13}$ and $\sqrt{G_v}G_v^{23}$), we used same discretization operator, as described in Sect. 2.3 of our paper. This strategy is beneficial to simply satisfy the geometric conservation law identity in the discretized equations. However, because the calculated geometric factors have the order p, it is possible to degrade the optimal convergence. Figures S1 (a), (b) show the spatial distribution of numerical errors for vertical wind and the local convergence rate, respectively, for $p = 3$. The numerical error is large near the surface where the mountain exists. Furthermore, the relatively slow convergence rate appears. The rate near the surface is about three, while it approaches the value of four at locations apart from the surface. Second, the modal filter can reduce the convergence rate during the long-term temporal integrations even if we adopted a high-order modal filter with a relatively small decay coefficient.

To increase the certainty of our speculations, we conducted additional numerical experiments. To simplify the investigations and save the computational resources, we treated the corresponding two-dimensional experimental setup. With respect to the Jacobian cofactors, we considered two cases: (i) the case where it is numerically given by using the same discretization operator mentioned in Sect. 2.3 of our paper, and (ii) the case when it is given by analytically evaluating the spatial derivatives at the node. In addition, to discuss the impact of modal filters
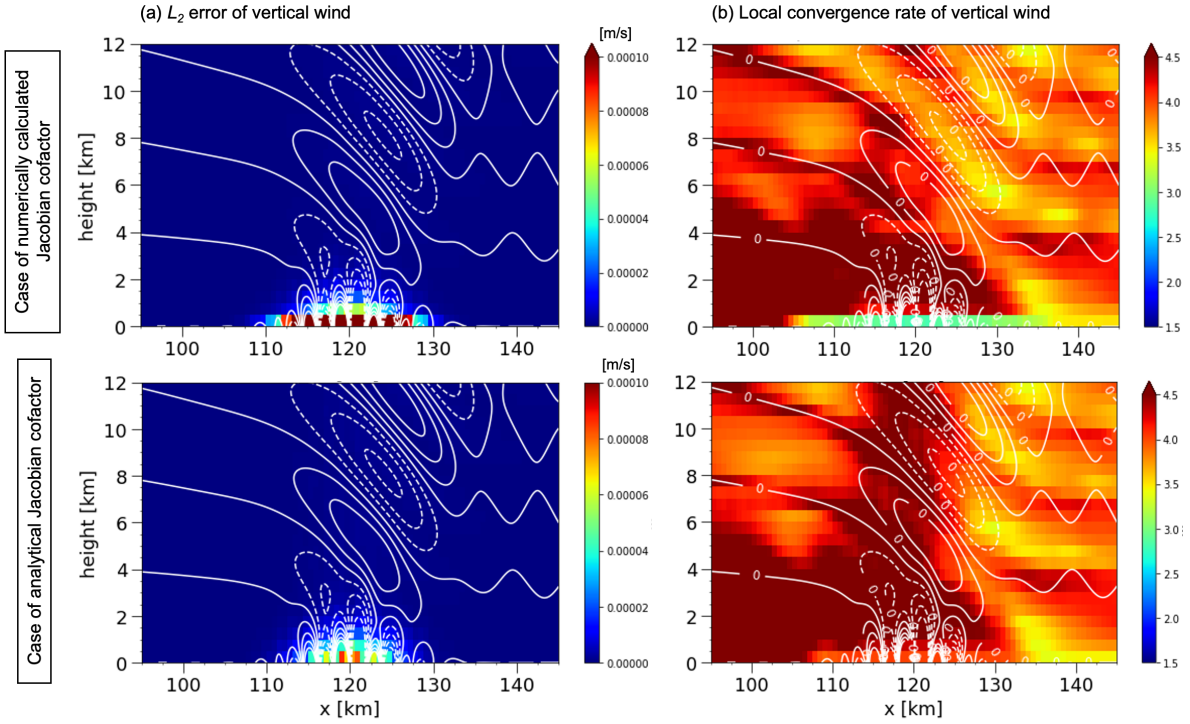
Figure S2: After 2 hours in a **two-dimensional** mountain wave test case, spatial distribution of (a) L_2 error norm and (b) local convergence rate for the vertical wind in the cases of numerically calculated Jacobian cofactor (upper panels) and analytical Jacobian cofactor (lower panels) for $p = 3$. In the L_2 error norm, we show the results obtained from the experiments with $\Delta_{\text{eff},h} = 156$ m and $\Delta_{\text{eff},v} = 125$ m. When evaluating the local convergence rare, we used the results obtained from two experiments: a coarse resolution experiment ($\Delta_{\text{eff},h} = 312$ m, $\Delta_{\text{eff},v} = 250$ m) and the highest resolution experiment for $p = 3$ ($\Delta_{\text{eff},h} = 39$ m, $\Delta_{\text{eff},v} = 31.25$ m). In each figure, the white lines represent the vertical wind in the reference experiment.

on the convergence rate, we consider the case of no modal filter for $p = 3$ because we found that the 2-hours temporal integration without filters can be somehow performed only for $p = 3$. As performed with the global model case, we conduct a series of numerical experiments changing the spatial resolutions and polynomial orders. To evaluate the error norms, we used the results from the reference experiments with $p = 7$, where $\Delta_{\text{eff},h} = 78$ m and $\Delta_{\text{eff},v} = 62.5$ m ($z < 15$ km).

1.3.1 Results from the two-dimensional experiments

Figures S2(a), (b) show the spatial distribution of numerical errors for vertical wind and the local convergence rate obtained from the two-dimensional experiments with $p = 3$. As shown in the global experiment (see Fig. S1), the convergence rate near the mountain achieves only the third-order accuracy in the cases of numerically calculated Jacobian cofactor. On the other hand, when the analytical Jacobian cofactor is used, the numerical errors near the mountain decrease and the convergence rate reaches to about fourth-order accuracy. Thus, we confirm that the calculation strategy of Jacobian cofactor is one of reasons for sub-optimal convergence.

Figure S3 shows that the dependence of L_1, L_2, and L_{inf} errors on the spatial resolution. First, we focus on the results with $p = 3$. When the metric cofactors are analytically evaluated and the modal filter is not used, the fourth-order accuracy is observed except for the density. In case of numerically calculated Jacobian cofactor, the convergence rate of L_2 and L_{inf} errors are characterized by the sub-optimal order because the Jacobian cofactors have only pth-order accuracy, as mentioned above. Such behavior is observed for horizontal wind, vertical
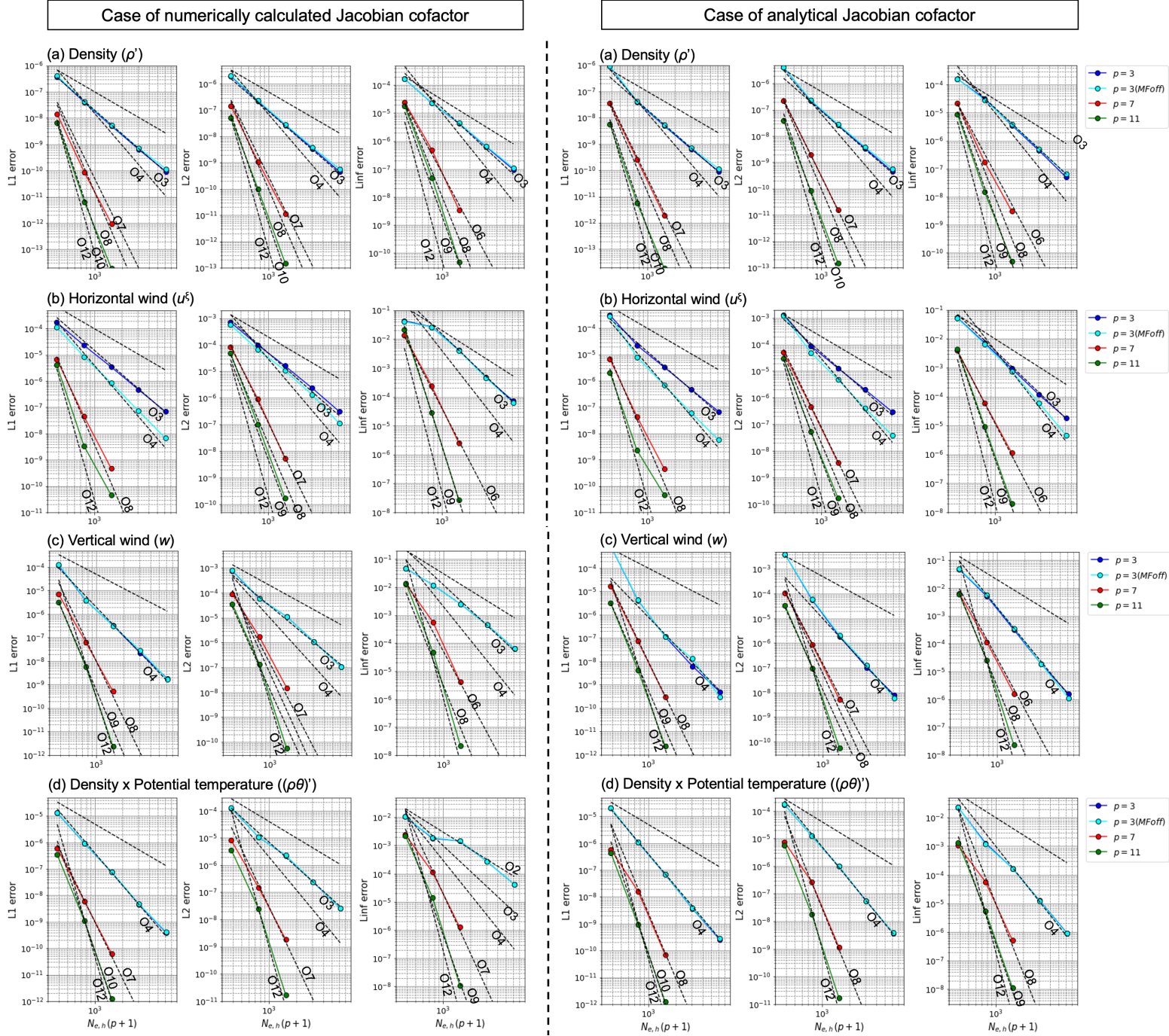
Figure S3: Dependence of L_1, L_2, and L_{inf} errors on spatial resolution for (a) density perturbation (ρ'), (b) horizontal wind (u^ξ), (c) vertical wind (w), and (d) perturbation of potential temperature weighted density (($\rho\theta)'$) after 2 hours in a mountain wave test case with the **two-dimensional experimental setup**. Note that the cyan lines represent the results for the case $p = 3$ without the modal filter (MFoff).

wind, and the perturbation of potential temperature weighted density based on the comparison between (i) and (ii) cases. On the other hand, the blue and cyan lines indicate that the order reduction with the modal filters is obvious for the horizontal wind, while for other variables, there is little influence. This may be because the filters act on not only the perturbation part of horizontal wind but also on the mean flow part. For higher order cases ($p = 7, 11$), the filters are unavoidable for ensuring numerical stability in classical DGM. Then, the convergence rate can be limited by the modal filters, and the analytical Jacobian cofactor would have little impact. Even for the case (ii), L_2 and L_{inf} errors of horizontal and vertical wind have the convergence rate slightly less than the optimal order. As for the density, note that the third-order accuracy is obtained for $p = 3$ even when using the analytical Jacobian cofactor and removing the modal filter. It remains unclear why the density error does not decrease in the optimal order. We may need to pursue how to discretely deal with the hydrostatic balance (e.g., Li and Xing 2018) and investigate the boundary errors with no-normal flux condition near the surface.

References

Gang Li and Yulong Xing. Well-balanced discontinuous galerkin methods with hydrostatic reconstruction for the euler equations with gravitation. *Journal of Computational Physics*, 352:445–462, 2018. ISSN 0021-9991.